Radio signals from axion star-neutron star binaries

Chris Kouvaris,[1] Tao Liu,[2] and Kun-Feng Lyu[3,2]

[1]*Physics Division, National Technical University of Athens, 15780 Zografou Campus, Athens, Greece*
[2]*Department of Physics, The Hong Kong University of Science and Technology, Clear Water Bay, Kowloon, Hong Kong SAR, People's Republic of China*
[3]*School of Physics and Astronomy, University of Minnesota, Minneapolis, Minnesota 55455, USA*

(Received 6 April 2022; revised 22 February 2023; accepted 12 December 2023; published 5 January 2024)

Axion stars could form binaries with neutron stars. Given the extremely strong external magnetic field exhibited by individual neutron stars, there can be a substantial conversion of axions to photons in these binaries. The photon emission is doubly modulated due to the neutron star spinning and the axion star orbiting, yielding a unique discovery signal. Similar features are also generated in binaries between a neutron star and an axion-clouded black hole. Encouragingly, such binaries are found to be within the reach of ongoing and upcoming experiments (e.g., the Five-hundred-meter Aperture Spherical Telescope and the future Square Kilometer Array) for certain parameter regions. They thus provide a promising astronomical laboratory for detecting axions and axion dark matter.

DOI: 10.1103/PhysRevD.109.023008

I. INTRODUCTION

Axions [1–7] and axionlike particles [8–10] (we will not distinguish them below) play a significant role in fundamental physics (for a recent review, see, e.g., [11]). For example, both of them can serve as a primary component of dark matter (DM), with a mass range spanning more than 20 orders of magnitude [12].

The axions interact with the Standard Model of particle physics feebly, with a strength generically suppressed by their decay constant. The detections of axions significantly rely on their Chern-Simons coupling,

$$\mathcal{L} \supset -c_\gamma \frac{\alpha_e}{4\pi f_a} a F_{\mu\nu} \tilde{F}^{\mu\nu}. \tag{1}$$

Here a is the axion field, m_a and f_a are its mass and decay constant, respectively, α_e is the fine-structure constant, $F_{\mu\nu}$ is the electromagnetic (EM) field strength, and $\tilde{F}_{\mu\nu}$ is its Hodge dual. The dimensionless coupling c_γ is model dependent. Its value can vary from $\sim\mathcal{O}(1)$ to many orders of magnitude higher [13–18]. In this context, a detection signal can be produced either in a static magnetic field, where a flux of axions are converted to photons via Primakoff process, or in a macroscopic axion field, where cosmological birefringence may occur when linearly polarized light travels across this field [12,19–21].

The extreme environment of stars is especially suitable for axion production and conversion. For example, the axions can be produced from the thermal photons in solar plasma or in core-collapsing supernovae such as SN1987A. These axions are then converted back to photons in an artificial or astrophysical magnetic field. The observations from the CERN Axion Solar Telescope and the Solar Maximum Mission satellite have set two of the most important constraints for the axion EM coupling [22–25]. In addition, the polarization measurements of cosmic microwave background [21,26,27] and pulsar light (with either individual pulsars [28,29] or pulsar polarization arrays [30]) provide a sensitive way to detect the axion field in certain mass regions.

Separately, in an axion-rich environment [e.g., in the early Universe or near black holes (BHs)], macroscopic objects such as axion miniclusters [31–35], axion clumps [36,37], and axion stars (ASs) [38] can form as a Bose-Einstein condensate, due to the effects of density fluctuations and self gravity (for recent reviews, see, e.g., [39,40]). The ASs can be either weakly bounded, known as dilute ASs, or compact as dense ones, depending on the concrete formation path. While traveling in space, these objects may collide with neutron stars (NSs) and then be substantially converted to radio signals in their magnetic fields, which are known to be extremely strong [41–48]. Furthermore, the AS can form a binary with the NS either by fragmentation, which pairs the AS and the supermassive progenitor of the NS from the start, or by late-time gravitational capture. Then as the AS is subjected to the NS strong magnetic field, the axions can be converted to photons in large numbers. The generated signals have double modulations with time due to the NS spinning and the AS Keplerian orbiting around the NS, thus yielding a signature which can unambiguously distinguish such a binary from the collision events and the other possible astrophysical radio sources.

Alternatively, the axions can form dense clouds surrounding a BH. "Gravitational atoms" (GAs) are such an

 © 2024 American Physical Society

example [49,50]. If the Compton wavelength of axions is comparable to the horizon of some spinning BH, the superradiance instability can occur [49–55], yielding a strong accumulation of axions at the BH "Bohr radius" and some other discrete orbitals by exacting the BH angular momentum and energy. Some other formation mechanisms also exist for the axion-clouded BH (ABH). For example, the axions if playing the role of DM could be part of an accretion disk around a BH [56–59]. Also, the axions could inhabit supermassive stars. They may survive a supernova blast and thus form a cloud around the newly born NS or BH (see, e.g., [60]).

In this paper we will examine three types of binaries, where the NS is accompanied by a (i) dilute AS (denoted as "AS1"), (ii) dense AS (denoted as "AS2"), and (iii) axion-clouded BH (denoted as "ABH"), respectively. We will demonstrate that the doubly modulating signals arising from these scenarios could be detected by the ongoing and upcoming experiments such as the Five-hundred-meter Aperture Spherical Telescope (FAST) [61,62] and the future Square Kilometer Array (SKA) [63,64].

II. BINARY PROFILE

The dilute ASs form where the axion number density is relatively small. They typically have a mass [65]

$$M_{\rm AS1} \lesssim 1.0\times 10^{-8} M_\odot \left(\frac{f_a}{10^{14}\ {\rm GeV}}\right)\left(\frac{10^{-6}\ {\rm eV}}{m_a}\right) \quad (2)$$

and a radius

$$R_{\rm AS1} \approx 2.7\ {\rm km}\left(\frac{10^{-8}M_\odot}{M_{\rm AS1}}\right)\left(\frac{10^{-6}\ {\rm eV}}{m_a}\right)^2. \quad (3)$$

In the dense case, the occupation number of axions is so big that their self-interactions, which are usually attractive, cannot be neglected. With a Thomas approximation, the radius of dense ASs is given by [65]

$$R_{\rm AS2} = 0.95\ {\rm m}\left(\frac{10^{14}\ {\rm GeV}}{f_a}\right)^{\frac{1}{2}}\left(\frac{10^{-6}\ {\rm eV}}{m_a}\right)^{\frac{1}{2}}\left(\frac{M_{\rm AS2}}{10^{-12}M_\odot}\right)^{0.3}. \quad (4)$$

The dense ASs are known as oscillons [66]. The lifetime of QCD axion oscillons is $\sim 10^3 m_a^{-1}$ [67–69]. The AS with such a short lifetime usually has little astrophysical and cosmological effects. However, it is not clear how long the longest possible lifetime for a general dense AS could be, which has been known to be highly dependent on the format of axion potential. For example, a flat or plateaulike potential may yield oscillons with a lifetime $> 10^{18} m_a^{-1}$ [70] or even of cosmological timescales [71]. As our goal is to present a perspective on the suggested signature, we will assume in this study that a certain amount of such ASs can survive until today.

We consider the GA as an ABH example. Its gravitational fine-structure constant α_G and Bohr radius r_G are defined as [72,73]

$$\alpha_G = G M_{\rm BH} m_a = 0.075\left(\frac{M_{\rm BH}}{10^{-5}M_\odot}\right)\left(\frac{m_a}{10^{-6}\ {\rm eV}}\right),$$
$$r_G = \frac{1}{m_a \alpha_G} = 2600\ {\rm km}\left(\frac{0.075}{\alpha_G}\right)\left(\frac{10^{-12}\ {\rm eV}}{m_a}\right). \quad (5)$$

Here α_G is required to be smaller than $\mathcal{O}(1)$ by the superradiance instability. For the GA $|211\rangle$ state (a leading growing mode of axion cloud), the maximally allowed value for its total mass (M_{211}) is constrained by $M_{211} \lesssim \min\{M_{\rm sat}, M_{\rm bos}\}$ [71,72,74], with

$$M_{\rm sat} \approx 1.5\times 10^{24}\ {\rm kg}\left(\frac{M_{\rm BH}}{10^{-5}M_\odot}\right)^2\left(\frac{m_a}{10^{-6}\ {\rm eV}}\right),$$
$$M_{\rm bos} \approx 0.42\times 10^{24}\ {\rm kg} \times \left(\frac{10^{-5}M_\odot}{M_{\rm BH}}\right)^3\left(\frac{10^{-6}\ {\rm eV}}{m_a}\right)^4\left(\frac{f_a}{10^{15}\ {\rm GeV}}\right)^2. \quad (6)$$

Here $M_{211} \lesssim M_{\rm sat}$ encodes the saturation condition, i.e., the angular momentum extracted from the spinning BH cannot be larger than its initial value [72], and $M_{211} \lesssim M_{\rm sat}$ comes from the bosenova limit [71,74], where the occupation number of axions ($N_{211} = M_{\rm bos}/m_a$) needs to be $\lesssim [10 f_a/(\alpha_G^{3/2} m_a)]^2$.

The NS spin with a period ranging from a few milliseconds to seconds. Normally, the magnetic field on their surface is $\lesssim 10^{12}$ G. But for magnetars, a class of extreme NSs, their magnetic field can reach $\sim 10^{15}$ G. For simplicity, we assume that the NS magnetic field is well approximated by a magnetic dipole $\vec{m}_{\rm NS}$ [75],

$$\vec{B}_{\rm NS}(\vec{r}) = -\frac{\mu_0}{4\pi}\frac{\vec{m}_{\rm NS} - 3(\vec{m}_{\rm NS}\cdot\hat{r})\hat{r}}{r^3}. \quad (7)$$

This is justified so long as the AS/ABH lies within the light cylinder of the NS which has a radius $r_c = c/\omega \simeq 4.8\times 10^4 T_s\ {\rm s^{-1}\,km}$ (T_s is the NS spin period).

The coordinate system used to describe the AS/ABH-NS binary is shown in Fig. 1. We assume the separation between the two objects of the binary to be sufficiently big, to neglect curvature corrections. We assume $M_{\rm NS} \gg M_{\rm AS/ABH}$ also, such that the NS stays at rest to a good approximation, while the AS/ABH orbits the NS with

$$r(\phi) = \frac{(1-e^2)r_0}{1+e\cos\phi_a}, \quad r_0 = \frac{l_0^2}{G M_{\rm NS}(1-e^2)}. \quad (8)$$

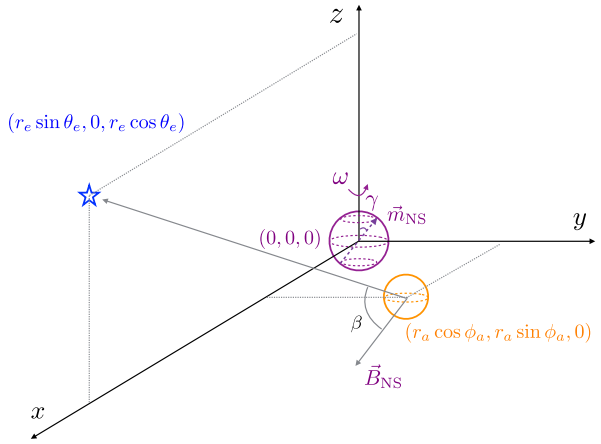

FIG. 1. Coordinate system used for describing the AS/ABH-NS binary. The purple and orange circles represent the NS and AS/ABH respectively, and the blue star represents Earth. The NS spins around the z axis with an angular velocity ω. Its magnetic dipole $\vec{m}_{\rm NS}$ is not aligned with its spin axis, subtending a misalignment angle γ. We have chosen this coordinate system such that the AS/ABH orbits the NS in its equator plane or the x–y plane, and Earth lies in the x–z plane.

Here e and r_0 are the orbit eccentricity and semimajor axis, l_0 is the AS/ABH angular momentum per unit mass, and ϕ_a is the AS/ABH azimuthal angle (see Fig. 1).

Let us give a rough estimate for the AS-NS binaries, following the corresponding estimate for the NS-NS binaries. The main mechanism to form a NS-NS binary which roughly agrees with the NS-NS merger rate observed in gravitational interferometers is related to the fact that ∼70% of stars form in binaries and out of them only ∼0.3% are supermassive and will evolve into a NS or a BH after supernova explosion. Given the average stellar density of the Universe $\sim 3\times 10^8 M_\odot/\mathrm{Mpc}^3$ and assuming the star formation rate for the last 10^{10} yr to be stable, we arrive at the typical binary formation rate of $\sim 200\ \mathrm{yr}^{-1}\,\mathrm{Gpc}^{-3}$ which is within the range expected for LIGO [76]. Here the probability for a binary to have two supermassive progenitors is $\sim(3\times 10^{-3})^2$. The reason that most stars form in binaries is related to a fragmentation process. As baryonic matter collapses, its density increases while its Jeans mass reduces. The molecular cloud thus gets fragmented. We will invoke a similar mechanism for the formation of the AS-NS binaries. We assume that, as baryons collapse, they draw into axions and ASs as well. The inner Milky Way (<20 kpc) contains $\mathrm{DM}\sim 1.4\times 10^{11} M_\odot$ [77]. Even if only ∼1% of DM is in the ASs [78] and with a mass of $10^{-8} M_\odot$ (typical for the dilute ASs), the AS population of the Galaxy is $\sim 1.4\times 10^{17}$. Note, the ASs are distributed in the DM halo of the inner Milky Way, while most stars ($\sim 10^{11}$) and NSs ($\sim 10^9$) of the Milky Way lie in the Galactic stellar disk (which has a radius of ∼15 kpc and a height of ∼300 pc [80]). The number of ASs contributing to the formation of AS-NS binaries is then $\sim 10^{17} V_{\rm disk}/V_{\rm halo}\sim 10^{15}$. Each supermassive progenitor for the stars will have $\sim 10^{15-11}=10^4$ ASs in its vicinity. Notably, the distribution of these axion stars is peaked around the host star, because of baryonic adiabatic contraction. As baryons collapse to form stars, they create a time-dependent gravitational potential that carries also the DM into the collapse center (see, e.g., [81,82]). The DM density with respect to the collapse center after the baryonic contraction then can be approximately described as [82]

$$\rho(r)=\frac{1}{4}\bar{\rho}\left(\frac{\bar{R}}{r}\right)^{9/4}. \tag{9}$$

In our context, $\bar{\rho}=10^4/(4/3\pi\bar{R}^3)$ represents the initial uniform distribution of ASs. $\bar{R}\sim(V_{\rm disk}/10^{11})^{1/3}$ denotes the average distance between two stars in the inner Milky Way. Here we have implicitly assumed that during the fragmentation each star collapses from a volume with a radius of $\bar{R}$. By integrating $\rho(r)$ over the space outside a NS with $1000<r<10^4$ km, which is our interest, and multiplying the NS number in the inner Milky Way, one can get $\sim 10^5$ AS-NS binaries. Given that the Roche limit is $\sim 10^3$ km for our parameter setup, this is approximately the number of stable binaries with a separation less than 10^4 km. These binaries evolve with time. Some of them might end up collapsing into the NS, but new such binaries will form also, as more and more ASs evolve to a distance below 10^4 km to their host star (since there are $\sim 10^4$ ASs per NS). This argument therefore indicates that it is possible to have many AS-NS binaries present in the Milky Way today. The SKA/FAST and other astronomical data in the near future may provide more messages or clues on their formation rate.

III. PHOTON EMISSION FROM THE BINARIES

The photon emission from the AS/ABH-NS binary is described by the axion-Maxwell equations, namely

$$\partial_\mu F_a^{\mu\nu}=j_a^\nu=-c_\gamma\frac{\alpha_e}{\pi f_a}\partial_\mu a\tilde{F}_{\rm NS}^{\mu\nu}. \tag{10}$$

Here $\tilde{F}_{\rm NS}^{\mu\nu}$ is the dual of the NS EM field strength, and $F_a^{\mu\nu}$ is the EM field strength induced by axion current. Using the retarded Green's function, one can find the vector potential near Earth and further the EM radiation power for the three types of binaries (see the Appendix for details),

$$\frac{dP_i}{d\Omega}=C_i\left(\frac{c_\gamma\alpha_e}{f_a}\right)^2|\vec{B}_{\rm NS}|^2\sin^2\beta, \tag{11}$$

where C_i is dimensionless, given by

$$C_{\rm AS1} = \frac{M_{\rm AS1}}{16\pi^4 m_a} v^3, \qquad C_{\rm AS2} = 4\frac{M_{\rm AS2} m_a^2 R_{\rm AS2}^3}{\pi^3 (1+m_a^2 R_{\rm AS2}^2)^4},$$
$$C_{\rm ABH} = \frac{1024\alpha_G^7 M_{211}}{(4+\alpha_G^2)^6 \pi^3 m_a} \sin^2\theta_e. \quad (12)$$

Here we have used the $1s$ wave function of hydrogen atoms to approximate the profile of dense ASs, following [44], and assumed the ABH to be in a $|211\rangle$ mode. θ_e is the polar angle of Earth's position (see Fig. 1). The spectral flux density is then derived by $S = \frac{dP}{d\Omega}(\mathcal{B} r_e^2)^{-1}$, where $\mathcal{B} \sim 0.1 m_a/2\pi$ is a conservative estimate on signal bandwidth, based on the Doppler effect.

Below let us consider three benchmark scenarios defined in Table I. We emphasize here that the plausibility of detection stands for orbital radii of $\mathcal{O}(10^3)$–$\mathcal{O}(10^4)$ km (as is indicated by our choice of $r_0 = 7.8 \times 10^3$ km for these scenarios). For a binary, its Roche limit sets up the minimal separation between its two objects, below which tidal forces will disrupt the relatively loose one. The Roche limit of, e.g., the AS1-BH binary, is given by

$$R_c \approx 1800 \left(\frac{M_{\rm NS}}{1.4 M_\odot}\right)^{\frac{1}{3}} \left(\frac{10^{-6}\,{\rm eV}}{m_a}\right)^{\frac{2}{3}} \left(\frac{10^{14}\,{\rm GeV}}{f_a}\right)^{\frac{4}{3}} {\rm km}, \quad (13)$$

which is several times smaller than the r_0 value. For lower f_a, the dilute AS becomes larger and R_c also increases.

Notably, the NS plasma deforms the dispersion relation of photons. The generated effective mass for photons, i.e.,

$$m_\gamma \sim w_p = \left(\frac{4\pi\alpha_e n_e}{m_e}\right)^{1/2}, \quad (14)$$

may have significant impacts on the EM radiation. Here w_p is the plasma frequency, m_e is the electron mass, and

$$n_e \sim 7 \times 10^{-2} \frac{B_{\rm NS}(r_a)}{1\ {\rm G}} \frac{1{\rm s}}{T_s}\ {\rm cm}^{-3} \quad (15)$$

is the electron number density in the magnetosphere [75]. If m_γ is comparable to or bigger than m_a, the axion-photon conversion will be enhanced or impeded [83–85]. This plasma effect cannot be ignored in the calculations then. In the benchmark scenarios, however, m_γ is $\sim 10^{-9}$ eV, safely below the axion mass $m_a = 10^{-6}$ eV.

Moreover, for these benchmark scenarios we consider a large value of 10^5 for the dimensionless Chern-Simons coupling c_γ. While such a choice is not minimal, it is theoretically well motivated. For example, a large c_γ can arise from biaxion model [16] and also clockwork theory [13–15]. More possibilities can be found in [18]. According to Eq. (11), the observational signals in these scenarios can be greatly strengthened for fixed f_a.

We show the spectral flux density for the AS1-NS benchmark binary (S_0) in Fig. 2. Due to the misalignment between the NS spin axis and magnetic dipole, the magnetic field at the AS/ABH orbit changes periodically. The generated signals are thus modulated by the NS spinning and the AS1 Keplerian orbiting, at relatively small and large timescales, respectively. For circular orbits,

TABLE I. Benchmark scenarios for the AS1-NS, AS2-NS, and ABH-NS binaries. The upper four rows show the parameter values shared by all three scenarios [except f_a which is taken to be $10^{14}(10^{15})$ GeV for the AS1/AS2(ABH)-NS binaries], the middle two rows summarize parameters specific to each scenario, and the bottom two rows gives the derived coefficients of radiation power in these scenarios [see Eq. (12)]. $M_{\rm NS}$, $R_{\rm NS}$, and $B_{\rm NS}^0$ are, respectively, the NS mass, radius, and magnetic field at the NS surface. T_o is the period of the AS/ABH revolution around the NS. As a condition for superradiance, the ABH mass $M_{\rm BH}$ has been assumed to have a value such that its horizon is comparable to the axion Compton wavelength.

$M_{\rm NS}$ ($M_\odot$)	$R_{\rm NS}$ (km)	$B_{\rm NS}^0$ (G)	γ (rad)	T_s (s)	T_o (s)
1.4	15	10^{12}	0.3	1.0	10
r_0 (km)	θ_e (rad)	r_e (kpc)	m_a (eV)	f_a (GeV)	T_o (s)
7.8×10^3	$\pi/4$	1.0	10^{-6}	$10^{14}(10^{15})$	10^5
$M_{\rm AS1}$ ($M_\odot$)	$R_{\rm AS1}$ (km)	$M_{\rm AS2}$ ($M_\odot$)	$R_{\rm AS2}$ (m)	$M_{\rm BH}$ ($M_\odot$)	M_{211} (kg)
10^{-8}	2.7	10^{-12}	0.95	10^{-5}	4.2×10^{23}
$v(e=0)$	$v(e=0.5)$	$C_{\rm AS1}$	$C_{\rm AS2}$	$C_{\rm ABH}$	
0.016	0.009–0.028	$7.2 \times 10^{60} v^3$	4.7×10^{55}	1.3×10^{55}	

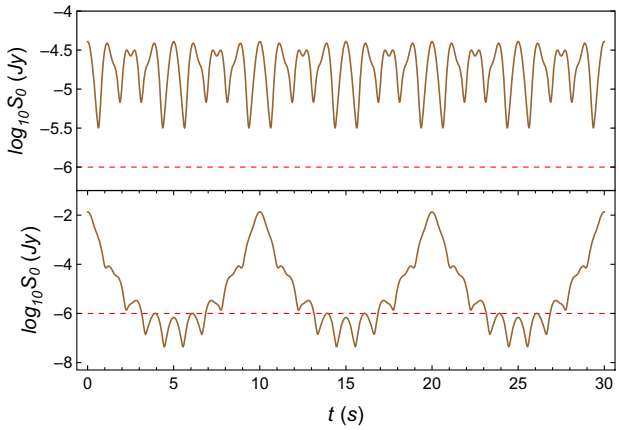

FIG. 2. Doubly modulated signals for the AS1-NS benchmark binary with $e = 0$ (upper) and 0.5 (lower). The red-dashed line represents a baseline sensitivity at the FAST and SKA, with one-hour observation [62,63]. As the benchmark binaries share the formula of radiation power in Eq. (11), the AS2-NS and ABH-NS time series signals can be obtained by scaling these AS1-NS curves by a factor $C_{\rm AS2}/C_{\rm AS1}$ and $C_{\rm ABH}/C_{\rm AS1}$ (for their values, see Table I), respectively. Note, a C_γ value of 10^5 has been assumed in these benchmark scenarios and also for the haloscope limits shown in Fig. 3.

the S_0 envelope is roughly flat on the top and described by a trigonometric function at the bottom. The NS spin adds a higher-frequency modulation due to its shorter period of $1s$. For elliptic orbits, the modulation is more pronounced because the AS1-NS separation changes periodically. When the AS1 gets close to its perihelion, the signals can be enhanced by orders of magnitude as the luminosity scales with the distance as $|\vec{B}_{\rm NS}|^2 \sim r^{-6}$.

The AS1-NS radio signals could be detected by the FAST and SKA. The FAST and SKA have a frequency coverage ranging from 70 MHz to 3 GHz, from 50 to 350 MHz (SKA-low), and 350 MHz to 14 GHz (SKA-mid), respectively, with a noise level $\lesssim O(1)$ μJy $(\mathrm{h}/t_{\rm obs})^{1/2}$ [62,63]. Here $t_{\rm obs}$ denotes observation time. The detectability of signals then can be simply estimated by comparing the magnitude of spectrum flux density and the noise level. Encouragingly, the spectral flux density presented in Fig. 2, i.e., S_0, lies above ($e = 0$) or mostly above ($e = 0.5$) the FAST/SKA noise level, with one hour of observation only. The doubly modulated signal patterns thus could be established with the data. We expect to achieve comparable sensitivities for detecting the AS2/ABH-NS benchmark binaries.

Finally, we show the spectral flux density (S) for the AS1-NS photon emission in Fig. 3. According to the discussions above, S scales with m_a and f_a as

$$S = \left(\frac{10^{-6}\ \mathrm{eV}}{m_a}\right)^3 \left(\frac{10^{14}\ \mathrm{GeV}}{f_a}\right) S_0. \tag{16}$$

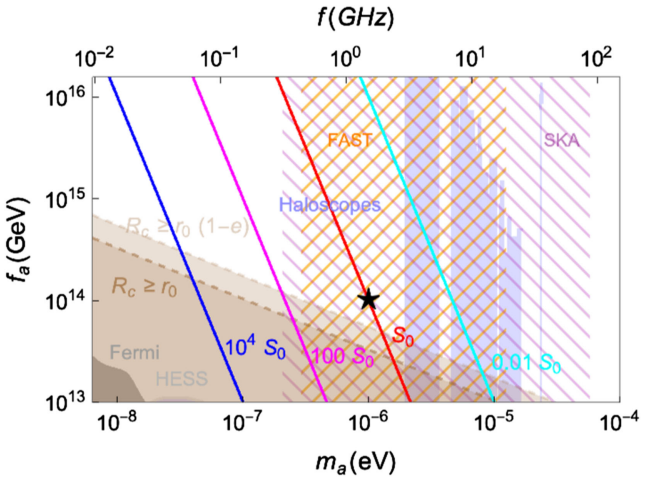

FIG. 3. Spectral flux density for the AS1-NS photon emission. The black star represents the benchmark scenario defined in Table I. The four different colored lines represent parameter points of constant signal strength as indicated. The light blue and gray regions have been excluded by the haloscope and FERMI/HESS observations, respectively [87]. The shaded brown and light brown regions are characterized by a Roche limit larger than the orbit radius ($e = 0$) and the perihelion ($e = 0.5$), respectively. The hatched regions denote the frequency coverage of FAST (orange) and SKA (purple).

Note, S_0 is not a constant. It represents a set of time-varying signals shown in Fig. 2. As shown in Fig. 3, S is enhanced quickly as m_a decreases. The low m_a region [i.e., $m_a \lesssim \mathcal{O}(10^{-7})$ eV] is difficult for terrestrial radio observations, due to the limitations such as ionospheric distortions and radio frequency interference of artificial signals. However, it could be well probed by future space- or lunar-based ultralow-frequency radio telescopes, whose frequency coverage is expected to reach sub-MHz, several orders of magnitude below the FAST and SKA low-frequency thresholds (see, e.g., [86]).

IV. CONCLUSION

In this paper we have studied the potential radio signals produced in the AS/ABH-NS binaries. In such systems, the extremely strong magnetic field of the NS can convert with a significant rate axions to photons. Due to the spinning of the NS as well as the Keplerian orbiting of the AS/ABH around the former, the radio-signal intensity is doubly modulated with time, yielding a striking discovery signature for the existence of the AS or the ABH in our galaxy. These signals also provide an astrophysical probe for axions that could shed light on the nature of DM. At last, we would stress that our proposal based on this study strongly responds to the current intensification of the observational efforts on radio frequencies and the coming of a new era for radio astronomy.

ACKNOWLEDGMENTS

K.-F. L. would like to thank Xi Tong, Qianhang Ding, and Hongyi Zhang for useful discussions. T. L. is supported by the Collaborative Research Fund under Grant No. C6017-20G which is issued by the Research Grants Council of Hong Kong SAR. K. F. L. is partially supported by the DOE Award No. DE-SC0022345.

APPENDIX: EM RADIATION FROM THE AS/ABH-NS BINARIES

With the axion's Chern-Simons coupling to the photon, we have the modified Maxwell equations

$$\partial_\mu F_a^{\mu\nu} = j_a^\nu = -\frac{c_\gamma \alpha_e}{\pi f_a} \partial_\mu a \tilde{F}_{\rm NS}^{\mu\nu}. \tag{A1}$$

Here $\tilde{F}_{\rm NS}^{\mu\nu}$ is the dual of the EM field strength generated by NSs, and $F_a^{\mu\nu}$ is the EM field strength induced by the axion current [44],

$$\begin{aligned} j_a^0 &= -\frac{c_\gamma \alpha_e}{\pi f_a} \nabla a \cdot \vec{B}_{\rm NS}, \\ \vec{j}_a &= \frac{c_\gamma \alpha_e}{\pi f_a} \left[(\partial_t a) \vec{B}_{\rm NS} + (\nabla a) \times \vec{E}_{\rm NS} \right]. \end{aligned} \tag{A2}$$

Recall that the four-vector EM potential is given by

$$A_a^\mu(t,\vec{r}_e) = \frac{1}{4\pi}\int_{V_a} d^3r \frac{j_a^\mu(\vec{r}, t-|\vec{r}_e-\vec{r}|)}{|\vec{r}_e-\vec{r}|} = \frac{1}{4\pi}\int_{V_a} d^3r' \frac{j_a^\mu(\vec{r}', t-|\vec{r}'_e-\vec{r}'|)}{|\vec{r}'_e-\vec{r}'|}. \quad \text{(A3)}$$

Here $\vec{r}_e$ and $\vec{r}$ in the first line denote the spatial coordinates of the observer and some point in the integral volume V_a, respectively, in the coordinate system defined in Fig. 1, while the variables with a prime in the second line refer to their counterparts in another coordinate system defined by shifting the original one to the AS or ABH center (such that $x' = x - r_a\cos\phi_a,\ y' = y - r_a\sin\phi_a,\ z' = z$). As $|\vec{r}_e| \gg |\vec{r}|_{V_a}$ and $|\vec{r}'_e| \gg |\vec{r}'|_{V_a}$, we have

$$r'_e = |\vec{r}'_e| \approx r_e = |\vec{r}_e|,$$
$$\hat{r}'_e \approx \hat{r}_e = \sin\theta_e\hat{x} + \cos\theta_e\hat{z} = \sin\theta_e\hat{x'} + \cos\theta_e\hat{z'}. \quad \text{(A4)}$$

In the nonrelativistic limit, the axion field can be decomposed as $a(t,\vec{r}') = a(\vec{r}')e^{-im_a t}$. Then, assuming the magnetic field strength near the AS or ABH $\vec{B}_{\rm NS}(t,\vec{r}')|_{V_a} \approx \vec{B}_{\rm NS}(t,\vec{r}'=0)$ and the electric field strength to be negligibly small, we obtain

$$A_a^0(t,\vec{r}_e) \approx -\frac{c_\gamma\alpha_e}{\pi f_a}\frac{e^{-im_a(t-r_e)}}{4\pi r_e} \times \vec{B}_{\rm NS}\cdot\int_{V_a} d^3r'\nabla' a(\vec{r}')e^{-im_a\hat{r}'_e\cdot\vec{r}'},$$
$$\vec{A}_a(t,\vec{r}_e) \approx \frac{-ic_\gamma\alpha_e}{\pi f_a}\frac{m_a e^{-im_a(t-r_e)}}{4\pi r_e} \times \vec{B}_{\rm NS}\int_{V_a} d^3r' a(\vec{r}')e^{-im_a\hat{r}'_e\cdot\vec{r}'}. \quad \text{(A5)}$$

The EM radiation power at the observer place (or Earth) finally can be calculated by

$$\frac{dP}{d\Omega} = \frac{1}{2}r_e^2{\rm Re}[\hat{r}_e\cdot(\vec{E}_a\times\vec{B}_a^*)] = \frac{1}{2}r_e^2 m_a^2|\vec{A}_a|^2\sin^2\beta, \quad \text{(A6)}$$

where β is the included angle between the NS external magnetic field $\vec{B}_{\rm NS}$ and the line of sight connecting Earth and the AS/ABH. In the following we will calculate the radiation power in the three benchmark scenarios.

1. AS1-NS binary

The dilute axion star AS1 is weakly bounded by gravitation, with a roughly constant energy density ρ_a. It is coherent within its de Broglie wavelength $d_a = 1/(m_a v)$. Here v is axion velocity. Following the idea in [44], one can divide the AS1 into a set of coherent patches, with a characteristic size d_a. The total radiation power of the AS1 in the NS external magnetic field is then given by

$$\frac{dP}{d\Omega} = \sum_i \frac{1}{2}\left(\frac{c_\gamma\alpha_e}{4\pi^2 f_a}\right)^2 a_i^2\frac{1}{m_a^2}\sin^2\beta|\vec{B}_{\rm NS}|^2 = \sum_i\left(\frac{c_\gamma\alpha_e}{4\pi^2 f_a}\right)^2\rho_{a,i}\frac{1}{m_a^4}\sin^2\beta|\vec{B}_{\rm NS}|^2 = \frac{V_a}{d_a^3}\left(\frac{c_\gamma\alpha_e}{4\pi^2 f_a m_a^2}\right)^2\rho_a\sin^2\beta|\vec{B}_{\rm NS}|^2 = \left(\frac{c_\gamma\alpha_e}{4\pi^2 f_a}\right)^2\rho_a V_a\frac{1}{m_a}v^3\sin^2\beta|\vec{B}_{\rm NS}|^2 = \left(\frac{c_\gamma\alpha_e}{4\pi^2 f_a}\right)^2\frac{M_{\rm AS1}}{m_a}v^3\sin^2\beta|\vec{B}_{\rm NS}|^2. \quad \text{(A7)}$$

Here a_i denotes the averaged field strength of axion in the ith patch. It is related to the axion energy density in this patch as $m_a^2 a_i^2/2 = \rho_{a,i} = \rho_a$. V_a defines the AS1 volume here and hence we have $M_{\rm AS1} = \rho_a V_a$.

2. AS2-NS binary

The AS2 as a dense axion star is much smaller than the AS1. It is coherent as a whole. Its profile can be approximately modeled by that of the electron cloud in an hydrogen atom [44], which gives

$$a(\vec{r}') = \frac{\sqrt{M_{\rm AS2}}}{m_a}\sqrt{\frac{2}{\pi}}\frac{1}{R_{\rm AS2}^{3/2}}e^{-r'/R_{\rm AS2}}. \quad \text{(A8)}$$

This profile has been normalized so that integrating over the whole space we can get the total mass $M_{\rm AS2}$, namely

$$\int_{V_a} d^3\vec{r}'\frac{m_a^2}{2}a(\vec{r}')^2 = M_{\rm AS2}. \quad \text{(A9)}$$

Then we have

$$\vec{A}_a \approx \frac{2c_\gamma\alpha_e}{f_a}\frac{e^{im_a(t-r_e)}}{\pi r_e}\sqrt{\frac{2}{\pi}}\frac{\sqrt{M_{\rm AS2}}R_{\rm AS}^{3/2}}{(1+m_a^2R_{\rm AS}^2)^2}\vec{B}_{\rm NS}, \quad \text{(A10)}$$

where $A_a^\mu(t,\vec{r}_e)$ is approximately independent of $\hat{r}'_e$ (it is also true for the AS1-NS binary), as the axion star profile is spherically symmetric [see Eq. (A8)]. The radiation power is finally given by

$$\frac{dP}{d\Omega} = 4\left(\frac{c_\gamma\alpha_e}{f_a}\right)^2\frac{M_{\rm AS2}m_a^2R_{\rm AS}^3}{\pi^3(1+m_a^2R_{\rm AS}^2)^4}|\vec{B}_{\rm NS}|^2\sin^2\beta. \quad \text{(A11)}$$

3. ABH-NS binary

For superradiance, the leading growing mode of axion cloud is $|211\rangle$. Its field configuration is described by [72]

$$a_{211}(t,\vec{r}') = \frac{1}{\sqrt{2m_a}}\left[\psi_{211}(t,\vec{r}')e^{-im_a t} + \psi^*_{211}(t,\vec{r}')e^{im_a t}\right], \tag{A12}$$

with

$$\psi_{211}(t,\vec{r}') \sim R_{21}(r')Y_{11}(\theta',\phi')e^{-i(\omega_{211}-m_a)t}. \tag{A13}$$

Here we have assumed the ABH to spin along the z' axis for simplicity. $|\omega_{211} - m_a| \ll m_a$ is the eigenenergy of the $|211\rangle$ state and can be neglected in the calculations below. Imposing the normalization condition which requests the axion-cloud total mass to be M_{211}, we then have

$$a_{211}(\vec{r}') = \frac{\sqrt{M_{211}}}{8\sqrt{2\pi}r_c^{5/2}m_a} r' e^{-\frac{r'}{2r_c}} \sin\theta' e^{i\phi'}. \tag{A14}$$

To find the vector potential $\vec{A}_a$, we calculate the integration in Eq. (A3) as

$$\begin{aligned}\int d^3r'\, a_{211}(\vec{r}')e^{-im_a\hat{r}'_e\cdot\vec{r}'} &= \int r'^2 dr'\, d\cos\theta' d\phi \frac{\sqrt{M_{211}}}{8\sqrt{2\pi}r_c^{5/2}m_a} r' e^{-\frac{r'}{2r_c}} \sin\theta' e^{i\phi} e^{-im_a\hat{r}'_e\cdot\vec{r}'} \\ &= \frac{\sqrt{M_{211}}}{8\sqrt{2\pi}r_c^{5/2}m_a}\int d\cos\theta' \sin\theta' \int dr' r'^3 e^{-\frac{r'}{2r_c}} \int d\phi e^{i\phi} e^{-im_a\hat{r}'_e\cdot\vec{r}'} \\ &= 96\sqrt{2\pi}\sqrt{M_{211}}r_c^{7/2}\int d\cos\theta' \frac{i\sin\theta'_e\sin^2\theta'\left[(i-2r_c m_a\cos\theta'_e\cos\theta')^2 + m_a^2 r_c^2\sin^2\theta'_e\sin^2\theta'\right]}{((i-2r_c m_a\cos\theta'_e\cos\theta')^2 - 4r_c^2 m_a^2\sin^2\theta'_e\sin^2\theta')^{7/2}} + \text{c.c.}\end{aligned} \tag{A15}$$

The integrated function in the last equality can be rewritten as

$$\frac{G(u)}{\left[4m_a^2r_c^2\left(u - \frac{i\cos\theta'_e}{2m_a r_c}\right)^2 - (4m_a^2r_c^2+1)\sin^2\theta'_e\right]^{7/2}}, \tag{A16}$$

with a replacement of $\cos\theta' \to u$ and $\sin\theta' \to \sqrt{1-u^2}$. Here $G(u)$ represents a sum of the polynomials of u, with a power up to 4. The integration in Eq. (A15) then can be calculated individually for these polynomials, yielding

$$F_n = \int_{-1-\frac{i\cos\theta'_e}{2m_a r_c}}^{1-\frac{i\cos\theta'_e}{2m_a r_c}} dw \frac{\left(w + \frac{i\cos\theta'_e}{2m_a r_c}\right)^n}{[4m_a^2r_c^2w^2 - (4m_a^2r_c^2+1)\sin^2\theta'_e]^{7/2}}, \tag{A17}$$

where $w = u - \frac{i\cos\theta'_e}{2m_a r_c}$ and $n = 0,\ldots,4$. With these inputs, we have

$$\vec{A}_a \approx \frac{32\sqrt{2}c_\gamma\alpha_e\sqrt{M_{211}}\alpha_G^{7/2}\sin\theta'_e}{(4+\alpha_G^2)^3 f_a\pi^{3/2}r m_a^{3/2}}\vec{B}_{\rm NS}e^{-im_a(t-r_e)}. \tag{A18}$$

The radiation power is finally given by

$$\frac{dP}{d\Omega} = \frac{1024\alpha_G^7 M_{211}c_\gamma^2\alpha_e^2}{(4+\alpha_G^2)^6 f_a^2\pi^3 m_a}|\vec{B}_{\rm NS}|^2\sin^2\theta'_e\sin^2\beta, \tag{A19}$$

where $\theta'_e \approx \theta_e$.

[1] R. Peccei and H. R. Quinn, Phys. Rev. Lett. **38**, 1440 (1977).
[2] R. Peccei and H. R. Quinn, Phys. Rev. D **16**, 1791 (1977).
[3] S. Weinberg, Phys. Rev. Lett. **40**, 223 (1978).
[4] F. Wilczek, Phys. Rev. Lett. **40**, 279 (1978).
[5] L. F. Abbott and P. Sikivie, Phys. Lett. **120B**, 133 (1983).
[6] J. Preskill, M. B. Wise, and F. Wilczek, Phys. Lett. **120B**, 127 (1983).
[7] M. Dine and W. Fischler, Phys. Lett. **120B**, 137 (1983).
[8] A. Arvanitaki, S. Dimopoulos, S. Dubovsky, N. Kaloper, and J. March-Russell, Phys. Rev. D **81**, 123530 (2010).
[9] P. Svrcek and E. Witten, J. High Energy Phys. 06 (2006) 051.
[10] M. Cicoli, M. Goodsell, and A. Ringwald, J. High Energy Phys. 10 (2012) 146.
[11] I. G. Irastorza and J. Redondo, Prog. Part. Nucl. Phys. **102**, 89 (2018).
[12] D. J. E. Marsh, Phys. Rep. **643**, 1 (2016).

[13] K. Choi and S. H. Im, J. High Energy Phys. 01 (2016) 149.
[14] D. E. Kaplan and R. Rattazzi, Phys. Rev. D **93**, 085007 (2016).
[15] G. F. Giudice and M. McCullough, J. High Energy Phys. 02 (2017) 036.
[16] P. Agrawal, J. Fan, M. Reece, and L.-T. Wang, J. High Energy Phys. 02 (2018) 006.
[17] A. J. Long, J. High Energy Phys. 07 (2018) 066.
[18] L. Di Luzio, M. Giannotti, E. Nardi, and L. Visinelli, Phys. Rep. **870**, 1 (2020).
[19] S. M. Carroll, G. B. Field, and R. Jackiw, Phys. Rev. D **41**, 1231 (1990).
[20] S. M. Carroll and G. B. Field, Phys. Rev. D **43**, 3789 (1991).
[21] D. Harari and P. Sikivie, Phys. Lett. B **289**, 67 (1992).
[22] CAST Collaboration, Nat. Phys. **13**, 584 (2017).
[23] K. Zioutas *et al.* (CAST Collaboration), Phys. Rev. Lett. **94**, 121301 (2005).
[24] S. Andriamonje *et al.* (CAST Collaboration), J. Cosmol. Astropart. Phys. 04 (2007) 010.
[25] C. G. Rapley, J. Sylwester, and K. J. H. Phillips, Sol. Phys. **292**, 50 (2017).
[26] N. F. Lepora, arXiv:gr-qc/9812077.
[27] A. Lue, L.-M. Wang, and M. Kamionkowski, Phys. Rev. Lett. **83**, 1506 (1999).
[28] T. Liu, G. Smoot, and Y. Zhao, Phys. Rev. D **101**, 063012 (2020).
[29] A. Caputo, L. Sberna, M. Frias, D. Blas, P. Pani, L. Shao, and W. Yan, Phys. Rev. D **100**, 063515 (2019).
[30] T. Liu, X. Lou, and J. Ren, Phys. Rev. Lett. **130**, 121401 (2023).
[31] M. Fairbairn, D. J. E. Marsh, J. Quevillon, and S. Rozier, Phys. Rev. D **97**, 083502 (2018).
[32] C. Hogan and M. Rees, Phys. Lett. B **205**, 228 (1988).
[33] L. Visinelli and J. Redondo, Phys. Rev. D **101**, 023008 (2020).
[34] B. Eggemeier, J. Redondo, K. Dolag, J. C. Niemeyer, and A. Vaquero, Phys. Rev. Lett. **125**, 041301 (2020).
[35] I. I. Tkachev, JETP Lett. **101**, 1 (2015).
[36] E. W. Kolb and I. I. Tkachev, Phys. Rev. D **50**, 769 (1994).
[37] M. P. Hertzberg, Y. Li, and E. D. Schiappacasse, J. Cosmol. Astropart. Phys. 07 (2020) 067.
[38] E. W. Kolb and I. I. Tkachev, Phys. Rev. Lett. **71**, 3051 (1993).
[39] H. Zhang, Symmetry **12**, 25 (2019).
[40] J. Eby, M. Leembruggen, L. Street, P. Suranyi, and L. C. R. Wijewardhana, Phys. Rev. D **100**, 063002 (2019).
[41] A. Iwazaki, Phys. Rev. D **91**, 023008 (2015).
[42] S. Raby, Phys. Rev. D **94**, 103004 (2016).
[43] M. S. Pshirkov, Int. J. Mod. Phys. D **26**, 1750068 (2017).
[44] Y. Bai and Y. Hamada, Phys. Lett. B **781**, 187 (2018).
[45] J. H. Buckley, P. B. Dev, F. Ferrer, and F. P. Huang, Phys. Rev. D **103**, 043015 (2021).
[46] Y. Bai, X. Du, and Y. Hamada, J. Cosmol. Astropart. Phys. 01 (2022) 041.
[47] S. Nurmi, E. D. Schiappacasse, and T. T. Yanagida, J. Cosmol. Astropart. Phys. 09 (2021) 004.
[48] J.-W. Wang, X.-J. Bi, and P.-F. Yin, Phys. Rev. D **104**, 103015 (2021).
[49] D. R. Brill, P. L. Chrzanowski, C. Martin Pereira, E. D. Fackerell, and J. R. Ipser, Phys. Rev. D **5**, 1913 (1972).
[50] S. L. Detweiler, Phys. Rev. D **22**, 2323 (1980).
[51] S. R. Dolan, Phys. Rev. D **76**, 084001 (2007).
[52] H. Yoshino and H. Kodama, Prog. Theor. Exp. Phys. **2014**, 043E02 (2014).
[53] R. Brito, V. Cardoso, and P. Pani, Lect. Notes Phys. **906**, 1 (2015).
[54] S. Endlich and R. Penco, J. High Energy Phys. 05 (2017) 052.
[55] W. E. East, Phys. Rev. Lett. **121**, 131104 (2018).
[56] T. Jacobson, Phys. Rev. Lett. **83**, 2699 (1999).
[57] L. K. Wong, A.-C. Davis, and R. Gregory, Phys. Rev. D **100**, 024010 (2019).
[58] K. Clough, P. G. Ferreira, and M. Lagos, Phys. Rev. D **100**, 063014 (2019).
[59] L. Hui, D. Kabat, X. Li, L. Santoni, and S. S. C. Wong, J. Cosmol. Astropart. Phys. 06 (2019) 038.
[60] C. Kouvaris and P. Tinyakov, Phys. Rev. D **82**, 063531 (2010).
[61] L. Zhu, in *Ground-Based and Airborne Telescopes VII*, edited by H. K. Marshall and J. Spyromilio, International Society for Optics and Photonics Vol. 10700 (SPIE, 2018), pp. 578–591, 10.1117/12.2309761.
[62] R. Nan, D. Li, C. Jin, Q. Wang, L. Zhu, W. Zhu, H. Zhang, Y. Yue, and L. Qian, Int. J. Mod. Phys. D **20**, 989 (2011).
[63] SKA baseline design document, https://www.skatelescope.org/wp-content/uploads/2014/03/SKA-TEL-SKO-0000308-SKA1-System-Baseline-v2-DescriptionRev01-part-1-signed.pdf (2015).
[64] A. Weltman *et al.*, Publ. Astron. Soc. Aust. **37**, e002 (2020).
[65] E. Braaten, A. Mohapatra, and H. Zhang, Phys. Rev. Lett. **117**, 121801 (2016).
[66] L. Visinelli, S. Baum, J. Redondo, K. Freese, and F. Wilczek, Phys. Lett. B **777**, 64 (2018).
[67] M. Gleiser, Phys. Rev. D **49**, 2978 (1994).
[68] P. Salmi and M. Hindmarsh, Phys. Rev. D **85**, 085033 (2012).
[69] G. Fodor, P. Forgacs, P. Grandclement, and I. Racz, Phys. Rev. D **74**, 124003 (2006).
[70] D. Cyncynates and T. Giurgica-Tiron, Phys. Rev. D **103**, 116011 (2021).
[71] M. A. Amin, A. J. Long, Z.-G. Mou, and P. Saffin, J. High Energy Phys. 06 (2021) 182.
[72] D. Baumann, H. S. Chia, R. A. Porto, and J. Stout, Phys. Rev. D **101**, 083019 (2020).
[73] D. Baumann, H. S. Chia, J. Stout, and L. ter Haar, J. Cosmol. Astropart. Phys. 12 (2019) 006.
[74] H. Yoshino and H. Kodama, Prog. Theor. Phys. **128**, 153 (2012).
[75] P. Goldreich and W. H. Julian, Astrophys. J. **157**, 869 (1969).
[76] E. Pian, Front. Astron. Space Sci. **7**, 108 (2021).
[77] L. Posti and A. Helmi, Astron. Astrophys. **621**, A56 (2019).
[78] In the early Universe, ∼10% axions are expected to be produced in the form of miniclusters usually (see, e.g., [35] and its references therein). Here we have taken a conservative estimate, assuming 1% of dark matter to be in the form of ASs. Similar strategy has also been taken in, e.g., [79], where 0.5% axion DM is assumed to be in the form of ASs.

[79] M. P. Hertzberg, E. D. Schiappacasse, and T. T. Yanagida, Phys. Rev. D **102**, 023013 (2020).
[80] J. Bland-Hawthorn and O. Gerhard, Annu. Rev. Astron. Astrophys. **54**, 529 (2016).
[81] F. Capela, M. Pshirkov, and P. Tinyakov, Phys. Rev. D **87**, 023507 (2013).
[82] G. Steigman, C. L. Sarazin, H. Quintana, and J. Faulkner, Astron. J. **83**, 1050 (1978).
[83] M. S. Pshirkov and S. B. Popov, J. Exp. Theor. Phys. **108**, 384 (2009).
[84] F. P. Huang, K. Kadota, T. Sekiguchi, and H. Tashiro, Phys. Rev. D **97**, 123001 (2018).
[85] A. Hook, Y. Kahn, B. R. Safdi, and Z. Sun, Phys. Rev. Lett. **121**, 241102 (2018).
[86] M. Bentum, M. Verma, R. Rajan, A. Boonstra, C. Verhoeven, E. Gill, A. van der Veen, H. Falcke, M. K. Wolt, B. Monna *et al.*, Adv. Space Res. **65**, 856 (2020).
[87] P. A. Zyla *et al.* (Particle Data Group), Prog. Theor. Exp. Phys. **2020**, 083C01 (2020).